6-14-2018

Efficient Phase Retrieval for Off-Axis Point Spread Functions

Salome Esteban Carrasco

EFFICIENT PHASE RETRIEVAL FOR OFF-AXIS POINT SPREAD FUNCTIONS

THESIS

S. Esteban Carrasco, CIV DR-II, USAF

AFIT-ENG-MS-18-J-084

DEPARTMENT OF THE AIR FORCE
AIR UNIVERSITY

AIR FORCE INSTITUTE OF TECHNOLOGY

Wright-Patterson Air Force Base, Ohio

AFIT-ENG-MS-18-J-084

EFFICIENT PHASE RETRIEVAL FOR OFF-AXIS POINT SPREAD FUNCTIONS

THESIS

Presented to the Faculty

Department of Electrical and Computer Engineering

Graduate School of Engineering and Management

Air Force Institute of Technology

Air University

Air Education and Training Command

in Partial Fulfillment of the Requirements for the

Degree of Master of Science in Electrical Engineering

S. Esteban Carrasco, B.S.O.E.

CIV DR-II, USAF

June 2018

AFIT-ENG-MS-14-J-084

EFFICIENT PHASE RETRIEVAL FOR OFF-AXIS POINT SPREAD FUNCTIONS

S. Esteban Carrasco, B.S.O.E
CIV DR-II, USAF

Committee Membership:

Dr. Stephen C. Cain
Chair

Maj Scott J. Pierce, PhD
Member

Dr. Michael Greiner
Member

Abstract

A novel pairing of phase retrieval tools allows for efficient estimation of pupil phase in optical systems from images of point spread functions (PSFs). The phase retrieval algorithm uses correlation of modeled phase in the focal plane to decouple aberrations that are difficult to identify in complex PSFs. The use of a phase kernel that departs from the Fresnel approximation for off-axis PSFs is a more accurate representation of wavefront phase in finite conjugate imaging. The combination of the approximation and phase correlation algorithm can be more efficient and accurate than generic algorithms.

Table of Contents

Page

List of Figures

List of Tables

List of Acronyms

Acronym	Definition
AFRL	Air Force Research Laboratory
AFIT	Air Force Institute of Technology
WPAFB	Wright Patterson Air Force Base
GS	Gerchberg-Saxton
PR	Phase Retrieval
PSF	Point Spread Function
FT	Fourier Transform
IFT	Inverse Fourier Transform
E-field	Electric Field
HST	Hubble Space Telescope
OTA	Optical Telescope Assembly
PC	Planetary Camera
GUI	Graphical User Interface

AFIT-ENG-MS-14-J-084

EFFICIENT PHASE RETRIEVAL FOR OFF-AXIS POINT SPREAD FUNCTIONS

S. Esteban Carrasco, B.S.O.E
CIV DR-II, USAF

Committee Membership:

Dr. Stephen C. Cain
Chair

Maj Scott Pierce, PhD
Member

Dr. Michael Greiner
Member

EFFICIENT PHASE RETRIEVAL FOR OFF-AXIS POINT SPREAD FUNCTIONS

I. Introduction

Analysis of an ideal optical system with paraxial geometrical optics theory results in the prediction of a perfect image free from any distortion or defect. However, physically realizable systems suffer additional effects that degrade the image quality. These degradations are called aberrations and they can be classified by their shape as departure from the desired wavefront or by effect on the image. To build a high quality system, a lens designer must minimize the aberrations in the system. Some aberrations may be attributed to the manufacturing techniques used to grind the glass lenses, misalignments, or loose tolerances in the lens curvatures. Aberrations are also caused by the shapes of the lenses, even if they were manufactured perfectly. For example, spherical aberration occurs for any lens with large enough diameter that its curvature causes the normal vectors of the lens surface to depart from the geometric approximations that would result in a perfect image. These errors can be corrected by using lenses ground to aspheric shapes that use polynomial descriptions to map its departure from a spherical surface. Another source of aberrations is the relative location of the source object to the optical system. If the object is very close to the system, the aperture of the system can experience variations in the incoming wavefront due to the range of propagation distances that exist from the object to the aperture. For example, an off-axis object will send out a wavefront that reaches one side of the aperture sooner than the other side of the aperture which would cause an aberration compared to a wavefront from an on-axis point.

In addition to aberrations, the most apparent effect on the system's performance is due to the aperture shape of the lens system. The shape and size of the aperture define the best

possible performance of the system. A system free from any of the aberrations mentioned above is often called a diffraction-limited system, meaning the diffractive effects of the pupil shape are the driving factors in image quality. An optical designer strives to limit aberrations to approach a diffraction-limited system.

As mentioned previously, aberrations cause a departure from a desired (flat) wavefront. The wavefront errors translate to phase differences in the light waves that travel through the system. A perfect system will take an incoming light wave, and alter the phase of the wave so that it focuses down to the focal plane. Characterizing any undesired phase differences leads to an understanding of the optical system and illustrates how the lens system must be changed to remove the phase errors and improve performance. Often a system with poor performance can be disassembled to have each individual lens tested for aberrations. However, in other situations, the system cannot be changed or examined directly and only the degraded imagery is available for analysis. In these cases, there is no direct solution for the phase of the light wave in the pupil plane of an optical system from imagery. A set of tools called phase retrieval algorithms are necessary to infer the phase (and therefore wavefront error) of the light from degraded images that contain no phase information. The depiction in Figure 1.1 shows how complex phase is lost when imaging with standard focal plane array (FPA) technology. Without a way to measure focal plane phase the pupil plane conditions are ambiguous and cannot be directly identified. Without an estimate of pupil phase, the aberrations in the system cannot be uniquely identified.

Consider the Camera Man image in Figure 1.2 as an example. The stock image is an array of pixels containing integer, real pixel values similar to the data captured by any conventional digital camera. There is no phase information in the original image. As an exercise, we apply two different phase distributions to the square root of the Camera Man image. One distribution consists of vertical bars taking the values of $-\pi, -\frac{\pi}{2}, \frac{\pi}{2}$, or π. The second phase distribution uses the same values, but distributed in a bull's eye

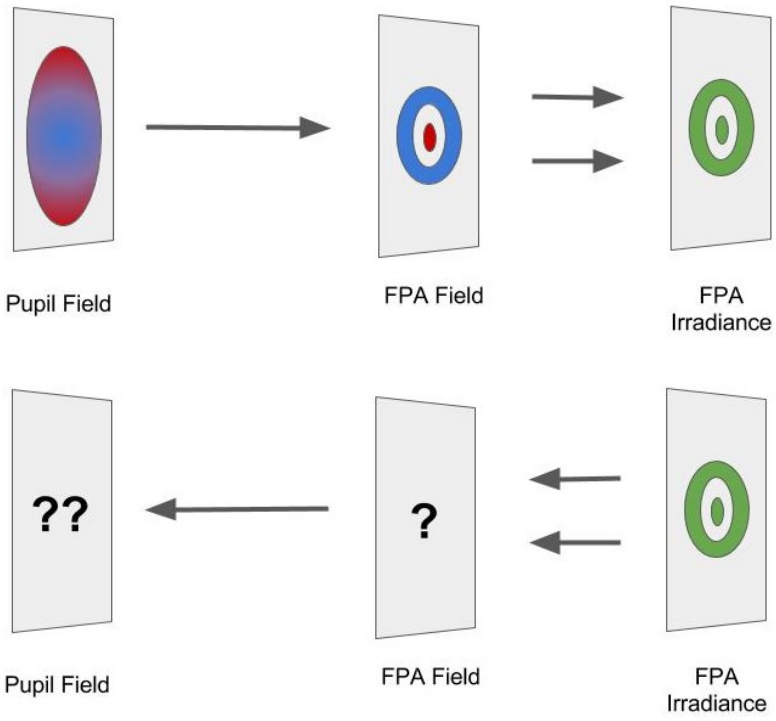

Figure 1.1. Top row: Magnitude and phase of the pupil field determines magnitude and phase in the focal plane. The squared magnitude of the focal plane field determines measurable irradiance but loses all phase information. Bottom row: In reverse, pupil phase cannot be directly recovered from an irradiance measurement.

pattern. The applied phase distributions do not change the magnitude of the simulated pixel values, just like how phase does not change the magnitude of an electric field as shown in Eq. (1.1). E_{CM} is the irradiance associated with the Camera Man Image and $|U_{CM}| = \sqrt{E_{CM}}$ representing the E-field magnitude. The example phase distributions are Φ_{bar} and $\Phi_{bullseye}$. Both phase distributions, when applied to field amplitude U_{CM} would generate identical Camera Man irradiance maps.

$$E_{CM} = UU^* = |U_{CM}e^{j\Phi_{bar}}|^2 = |U_{CM}e^{j\Phi_{bullseye}}|^2 \tag{1.1}$$

In a real experiment, the measured pixel values are proportional to the irradiance incident on the camera and therefore are also proportional to the squared magnitude of the E-field in the focal plane. By augmenting the square root of the simulated Camera Man image pixels with the aforementioned phase distributions we are simulating two possible E-fields that create the Camera Man Image. Since the phase in the original Camera Man image was lost upon detection, either of our simulated phase distributions could be mathematically valid. The next sections will describe the physics in greater detail, but for now consider that the propagation of E-fields in an optical system can be modeled with a FT. Taking the inverse Fourier transform of the Camera Man image combined with the hypothetical bar and ring phase distributions yields the E-field magnitudes in Figure 1.3. Notice the different structure in the resultant E-field magnitudes, which are more apparent when imaging on a logarithmic scale. The same Camera Man image with different phase distributions will give radically different FTs. The output of a Fourier transform is highly dependent on the input image's phase. Without being able to directly measure phase in the focal plane one cannot distinguish between the infinite number of phase distributions that are able to create the same irradiance pattern.

The remaining chapters of this document are organized as follows: Chapter II gives background about phase retrieval techniques and derives the relationships that phase retrieval algorithms exploit. Chapter 3 discusses the methodology used in the presented algorithm, including a flow chart of the algorithm, the implementation of the algorithm in MATLAB, and the application of a special propagator for off-axis imagery. Chapter 4 includes the results of the algorithm when applied to synthetic test data and to experimental data. Chapter 5 provides a conclusion of this work.

(a)

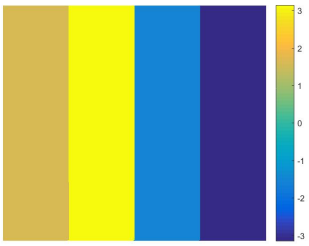

(b)

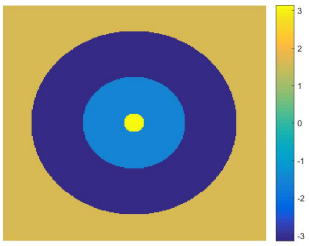

(c)

Figure 1.2. (a) The Camera Man example image, (b) a vertical phase distribution, (c) a bull's eye phase distribution.

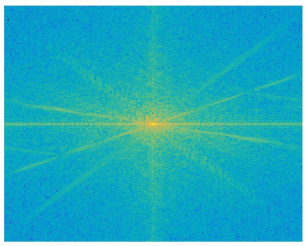

(a)

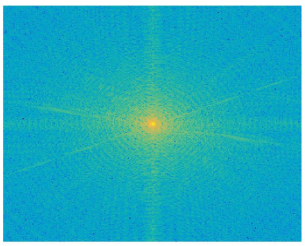

(b)

Figure 1.3. Transform pairs of the Camera Man combined with phase distributions from the previous figure: (a)log scale magnitude of the FT of the vertical distribution, and (b) log scale magnitude of the FT of the bull's eye distribution.

II. Phase Retrieval Background

2.1 Derivation of Fresnel Integral

Phase retrieval is the process used to recreate the complex phase component of the electromagnetic light field in the pupil plane of an optical system. Phase in the pupil plane of an optical system can be retrieved from the system's prescription (entrance pupil diameter, focal length, etc.) and from irradiance measurements of the the system's Point Spread Function (PSF). No phase information is captured whatsoever in the PSF, only a quantity of photoeletric counts proportional to the squared magnitude of incident field. If it were possible to measure the field phase in the focal plane, it would be easier to retrieve the phase in the pupil plane. However, using current technology, we are limited to sensors that cannot measure phase. The mathematics and physics that relate the amplitude and phase of a light wave to an image at a focal plane are not one-to-one processes; an infinite number of complex pupil functions can give rise to the same fully real PSF. To illustrate this, we will build the Fourier propagation approximation.

The Rayleigh-Sommerfeld approximation, shown in Eq. (2.1), governs the propagation of light fields between two planes. As shown, the temporally independent complex field is $U(x, y, 0)$,where x and y are transverse to the direction of propagation, and the input plane is defined at $z = 0$ for simplicity. The field will propagate to a point (ξ, η, z) in the second plane as a summation of point sources that radiate as spherical waves modeled by $\exp\left(j\frac{2\pi}{\lambda}R\right)$, where $R = \sqrt{(\xi - x)^2 + (\eta - y)^2 + z^2}$ and is the distance between the points in the two planes. The Rayleigh-Sommerfeld approximation adds an additional directional component $\cos(\chi) \approx \frac{z}{R}$, phase lag $\frac{1}{j}$, and wavelength scaling $\frac{1}{\lambda}$ to accurately describe the evolution of the field from one plane to another [9].

$$U(\xi, \eta, z) = \frac{z}{j\lambda} \int_x \int_y U(x, y, 0) \frac{\exp(j2\pi \frac{R(x,y,\xi,\eta)}{\lambda})}{R^2(x, y, \xi, \eta)} dxdy \tag{2.1}$$

A simplifying approximation is made by expanding the term for radial distance within the phase kernel. If the propagation distance between the planes, z, is much greater than the transverse dimensions of the planes, x and y, we are left with Eq. (2.2).

$$R(\xi,\eta,x,y,z) \approx z + \frac{(x-\xi)^2+(y-\eta)^2}{2z} \approx z + \frac{x^2+y^2}{2z} + \frac{\xi^2+\eta^2}{2z} - \frac{x\xi+y\eta}{z} \tag{2.2}$$

Inserting Eq. (**??**) into Eq. (2.1), with an additional paraxial assumption that terms outside of the exponential phase kernel can be approximated by $z \approx R$ gives Eq. (2.3) which is recognizable as the Fresnel propagation integral [9].

$$U(\xi,\eta,z) \approx \frac{\exp\left(j\pi\frac{\xi^2+\eta^2+2z^2}{\lambda z}\right)}{j\lambda z}\int_x\int_y U(x,y,0)\exp\left(j\pi\frac{x^2+y^2}{\lambda z}\right)\exp\left(-j2\pi\frac{x\xi+y\eta}{\lambda z}\right)dxdy \tag{2.3}$$

Since current detectors are limited to measurements of field irradiance, many of the complex terms outside of the integral can be dropped for simplicity when simulating focal plane imagery. Additionally, PSFs are typically normalized, so absolute amplitude is not vitally important and scaling coefficients can be discarded as well. A final approximation, that the source phase curvature $\exp\left(j\pi\frac{x^2+y^2}{\lambda z}\right)$ is invariant leaves a simplified Fraunhofer (or Fourier) propagator shown in Eq. (2.4). The propagator involves a Fourier transform of the source coordinate plane into an image coordinate frame scaled by the geometry of the propagation and the wavelength of light. This transform relationship is at the center of this work's phase retrieval algorithm.

$$U(\xi,\eta,z) \approx \mathcal{F}\left[U(x,y,0)\right] \tag{2.4}$$

2.2 Zernike Polynomials

The work above shows the relationship between pupil phase and a PSF. It can be useful to have a method of quantifying any deviations from a perfectly flat wavefront.

To break down and quantify the wavefront, a set of functions called Zernike polynomials are used. Zernike polynomials are a set of orthogonal functions over a unit disk. [10] The shape of these polynomials is convenient for their use in optics, as the clear aperture of spherical lenses is typically circular. The orthogonality of the functions allows for an efficient reconstruction of the residual phase error by decomposing the error into a set of coefficients. In this case, orthogonality is the feature that the inner product of one Zernike polynomial with any other is zero. Each Polynomial term contains a unique portion of the information that builds the wavefront error. By using a set of standard polynomials modified by a matching set of weighting coefficients one can approach a nearly complete approximation of the original wavefront error. For this work, the ordered list of polynomials is shown in Table 2.1. The indexing does not follow the OSA/ANSI numbering scheme, but instead is ordered by radial, and then by azimuthal index.

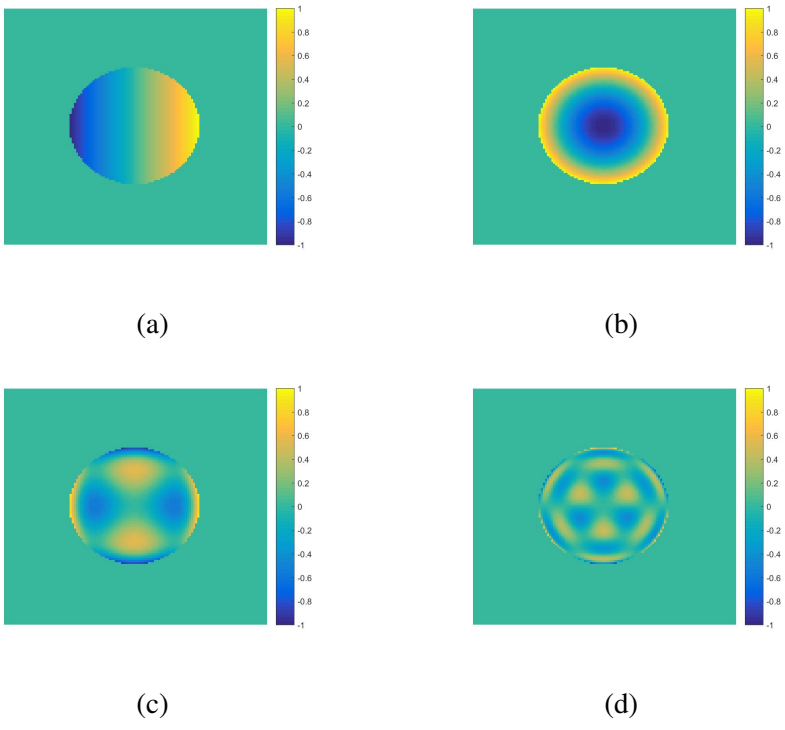

Figure 2.1. Example Zernike Polynomials from Table 2.1 (a) Z2, (b) Z4, (c) Z12, (d) Z44.

Table 2.1: Table of Zernike Polynomials

1	1
2	$\rho\cos(\theta)$
3	$\rho\sin(\theta)$
4	$-1+2\rho^2$
5	$\rho^2\cos(2\theta)$
6	$\rho^2\sin(2\theta)$
7	$\rho(-2+3\rho^2)\cos(\theta)$
8	$\rho(-2+3\rho^2)\sin(\theta)$
9	$1-6\rho^2+6\rho^4$
10	$\rho^3\cos(3\theta)$
11	$\rho^3\sin(3\theta)$
12	$\rho^2(-3+4\rho^2)\cos(2\theta)$
13	$\rho^2(-3+4\rho^2)\sin(2\theta)$
14	$\rho(3-12\rho^2+10\rho^4)\cos(\theta)$
15	$\rho(3-12\rho^2+10\rho^4)\sin(\theta)$
16	$-1+12\rho^2-30\rho^4+20\rho^6$
17	$\rho^4\cos(4\theta)$
18	$\rho^4\sin(4\theta)$
19	$\rho^3(-4+5\rho^2)\cos(3\theta)$
20	$\rho^3(-4+5\rho^2)\sin(3\theta)$
21	$\rho^2(6-20\rho^2+15\rho^4)\cos(2\theta)$
22	$\rho^2(6-20\rho^2+15\rho^4)\sin(2\theta)$
23	$\rho(-4+30\rho^2-60\rho^4+35\rho^6)\cos(\theta)$
24	$\rho(-4+30\rho^2-60\rho^4+35\rho^6)\sin(\theta)$
25	$1-20\rho^2+90\rho^4-140\rho^6+70\rho^8$
26	$\rho^5\cos(5\theta)$
27	$\rho^5\sin(5\theta)$
28	$\rho^4(-5+6\rho^2)\cos(4\theta)$
29	$\rho^4(-5+6\rho^2)\sin(4\theta)$
30	$\rho^3(10-30\rho^2+21\rho^4)\cos(3\theta)$
31	$\rho^3(10-30\rho^2+21\rho^4)\sin(3\theta)$
32	$\rho^2(-10+60\rho^2-105\rho^4+56\rho^6)\cos(2\theta)$
33	$\rho^2(-10+60\rho^2-105\rho^4+56\rho^6)\sin(3\theta)$
34	$\rho(5-60\rho^2+210\rho^4-280\rho^6+126\rho^8)\cos(\theta)$
35	$\rho(5-60\rho^2+210\rho^4-280\rho^6+126\rho^8)\sin(\theta)$
36	$-1+30\rho^2-210\rho^4+560\rho^6-630\rho^8+252\rho^10$
37	$\rho^6\cos(6\theta)$
38	$\rho^6\sin(6\theta)$
39	$\rho^5(-6+7\rho^2)\cos(5\theta)$
40	$\rho^5(-6+7\rho^2)\sin(5\theta)$
41	$\rho^4(15-42\rho^2+28\rho^4)\cos(4\theta)$
42	$\rho^4(15-42\rho^2+28\rho^4)\sin(4\theta)$
43	$\rho^3(-20+105\rho^2-168\rho^4+84\rho^6)\cos(3\theta)$
44	$\rho^3(-20+105\rho^2-168\rho^4+84\rho^6)\sin(3\theta)$
45	$\rho^2(15-140\rho^2+420\rho^4-504\rho^6+210\rho^8)\cos(2\theta)$
46	$\rho^2(15-140\rho^2+420\rho^4-504\rho^6+210\rho^8)\sin(2\theta)$
47	$\rho(-6+105\rho^2-560\rho^4+1260\rho^6-1260\rho^8+462\rho^10)\cos(\theta)$
48	$\rho(-6+105\rho^2-560\rho^4+1260\rho^6-1260\rho^8+462\rho^10)\sin(\theta)$

2.3 Iterative Phase Retrieval Methods

After illustrating the Fourier pair relationship between fields in the pupil and focal plane we can introduce one of the major types of phase retrieval algorithms, the Gerchberg-Saxton (GS) Algorithm. The GS algorithm is an iterative algorithm that uses successive Fourier transforms (FTs) and inverse Fourier transforms (IFTs) to estimate phase in the pupil [7]. As shown in Figure 2.2, first a set of PSF data is measured at the FPA of the

optical system. Then, the square root of the data is given a randomly generated phase for each pixel. The random phase is used to initialize the imaginary portion of the image field estimate, while the square root of the target PSF constrains the image field magnitude. This complex estimate at the FPA is run through an IFT for an estimate of the pupil plane field. However, the solution for the pupil plane field may not match the physical properties of the system. Using knowledge of the pupil's shape and illumination, the result of the IFT is truncated to match the known pupil of the optical system. In this way some phase information is kept but the spatial distribution of the pupil estimate matches the true system. Now that the pupil has been reshaped it is run through another FT, giving a new estimate for the image field in the FPA. The phase of this estimate is kept, but the magnitude is replaced with the square root of the target PSF. The steps described above constitute a single iteration of the GS algorithm. The process is repeated until the estimate of pupil phase stabilizes. This method is simple and easy to implement [5], but has limited utility as the estimate can oscillate and vary wildly with each iteration. Additionally, the output of the GS will require an unwrapping algorithm if the phase values exceed $\pm\pi$ before the phase contour can be decomposed into Zernike Polynomials.

Other methods have been developed to improve upon the GS algorithm by selectively applying the constraint criteria. For instance, the "input-output" method does not globally apply the constraint parameters, but instead applies a weighted perturbation to any region of the image that has not satisfied the criteria. Any pixel that violates the condition will be set to its initial value, minus the output produced by the offending initial value [6]. In this way the estimate can be driven towards the desired conditions more smoothly while escaping local minima solutions.

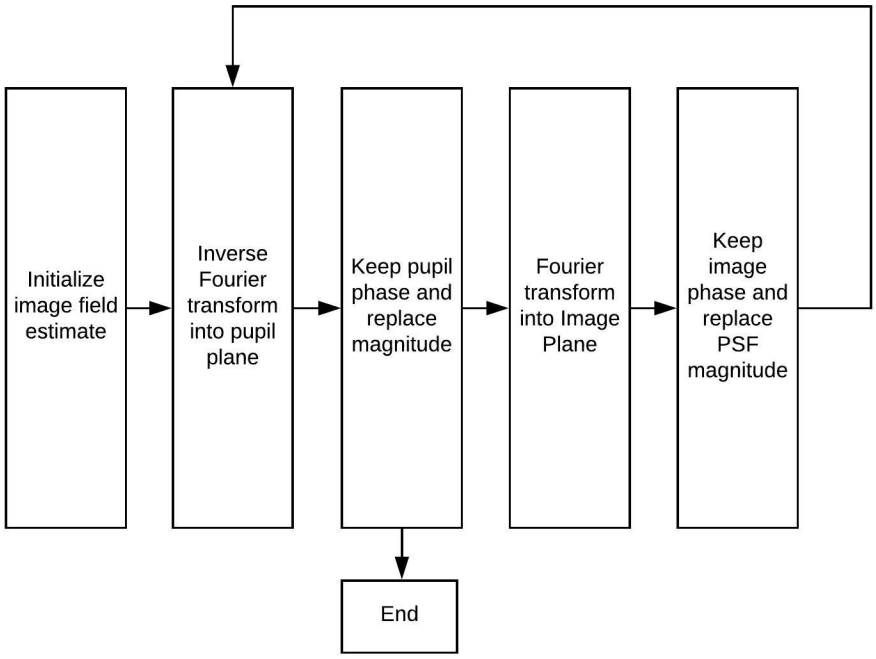

Figure 2.2. Generic Gerchberg-Saxton algorithm.

2.4 Gradient Descent Phase Retrieval Methods

Another important type of phase retrieval algorithm is the gradient-descent, or parametric search method. These algorithms also take advantage of the Fourier relationship between image and pupil, but they do not let the phase estimate float freely during the solution. Instead they parameterize the phase, typically with Zernike polynomials, and search for the combination of parameters that minimize some error function. The error function is typically a weighted difference between the PSF estimated by the parameterized pupil and a target PSF captured with the optical system of interest. When the estimate's error function has reached a minimum, the algorithm is stopped and phase coefficients are reported. These algorithms also fall victim to local minima, where every increment or perturbation from the current estimate results in greater error. With current computing power these searches are handily accomplished, but when first introduced these algorithms

were solved by deriving the partial derivatives with respect to the wavefront parameters and using the analytic gradients for the basis of a computational search [3]. Today, computing resources allow for the simulation of multiple pupil/PSF pairs for dozens of Zernike coefficients.

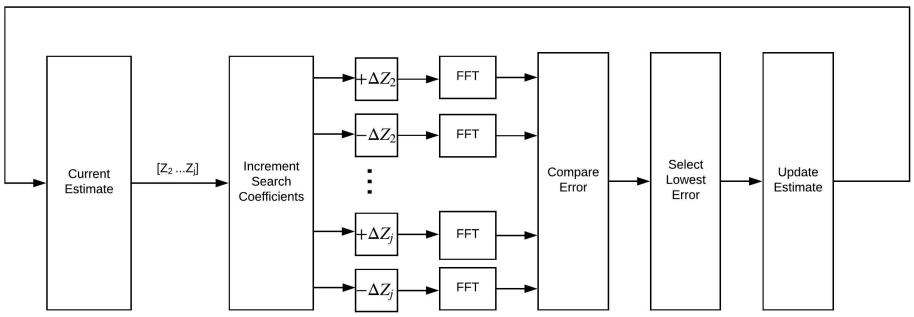

Figure 2.3. Generic gradient descent algorithm.

2.5 Applications of Phase Retrieval

Although phase retrieval also has applications in x-ray crystallography, electron microsocpy, and other areas [11], this work will focus on its use in optical imaging. Phase retrieval can be used to improve terrestrial telescope imagery. Atmospheric turbulence adds distortion that lowers the Strehl Ratio, a measure of a system's proximity to a diffraction-limited system, for an Earth-based telescope. An additional technique called Phase Diversity can add a degree of control over the algorithm by comparing two images with a known difference in pupil phase that helps anchor the estimate. This diversity can be achieved by a slight defocus between the images, either by taking a defocused image immediately after a focused image, or by splitting the final leg of the optical system with a beam splitter to two separate focal planes. Another method is sequential diversity imaging, where an adaptive optic system continuously cancels and adds phase at a rate faster than

the turbulence changes. The temporally separated frames can be used as phase diversity estimates to achieve a higher image resolution by negating the atmospherically induced aberrations [8].

Phase retrieval algorithms were famously used in the effort to repair the Hubble Space Telescope (HST) after it came on-line. [4]. The first images from the HST had lower resolution than expected, with an encircled energy radius 7 times higher than the specification. With the HST already on orbit, it would be nearly impossible to physically inspect the Optical Telescope Assembly (OTA) to diagnose the issue. Several different cameras were installed on the HST and all of them depended on the OTA and therefore suffered from poor performance. The Planetary Camera (PC) in particular was particularly well suited for phase retrieval. The PC's wavelength filters meant that the pupil/FPA sampling conditions were adequately met and the PC's noise characteristics provided imagery with suitable signal to noise ratio [4]. The Hubble Aberration Recovery Program used multiple analyses from the PC imagery along with other tools to identify that a grinding error in the primary mirror resulted in spherical aberration that degraded the images. The error was roughly $2\mu m$ of difference over the 7.8m mirror. The entire operation from identification to correction took 3 years [8].

Fienup's account of the phase retrieval study gives insight into the difficulties of applying these techniques. The 22 coefficient solution for pupil phase required multiple propagation steps through the system, rather than one full propagation from entrance pupil to FPA. The multiple propagations allowed smaller array sizes for more efficient computations and allowed for a better simulation of the obscurations in the pupil from the arms of the secondary mirror. However, even with the multiple propagations the simulation required the addition of imaginary elements to cancel and reintroduce quadratic phase that varied too rapidly to be sampled [4]. The analysis showed that there was a misalignment between the OTA and the PC and that some of the telescope's parameters were not known

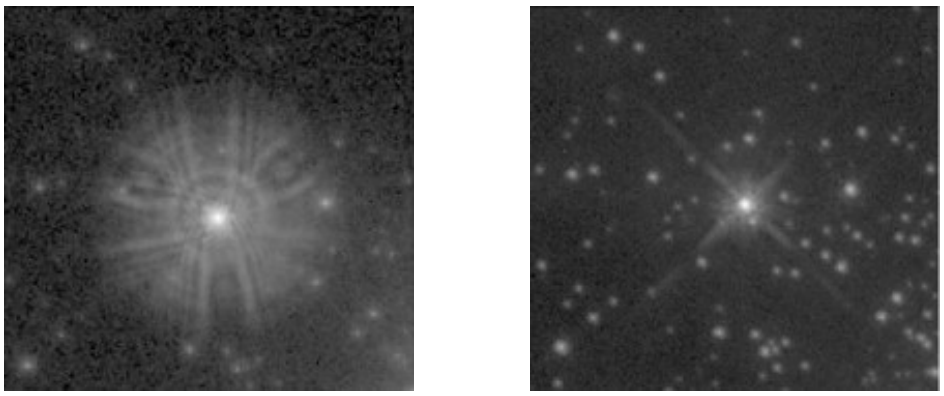

(a) (b)

Figure 2.4. Hubble Space Telescope imagery (a) before, and (b) after correction.

with the accuracy required for simulation. The paper shows that minute changes in the scaling between the FPA pixels and the field of view can change the magnitude of the retrieved aberration. Knowing the system parameters more accurately can provide a better fit to experimental data. Phase retrieval algorithms could not be applied to the HST problem without some effort, but the results shown in Figure 2.4 clearly prove the technique's efficacy [1].

III. Methodology

3.1 Phase Retrieval Algorithm

The phase retrieval algorithm presented in this work is derived from one published by Zingarelli and Cain [12]. The iterative approach begins with an estimate of the field amplitude in the FPA by use of the GS Algorithm, as shown in Figure 3.1. The pupil phase initializing the GS algorithm is parameterized by Zernike coefficients shown in the diagram as $[Z_2...Z_j]^N$. After 20 iterations of the GS transform, the phase component of the GS output is combined with the square root of the target PSF to create a complex E-field model that is passed to the next section of the algorithm.

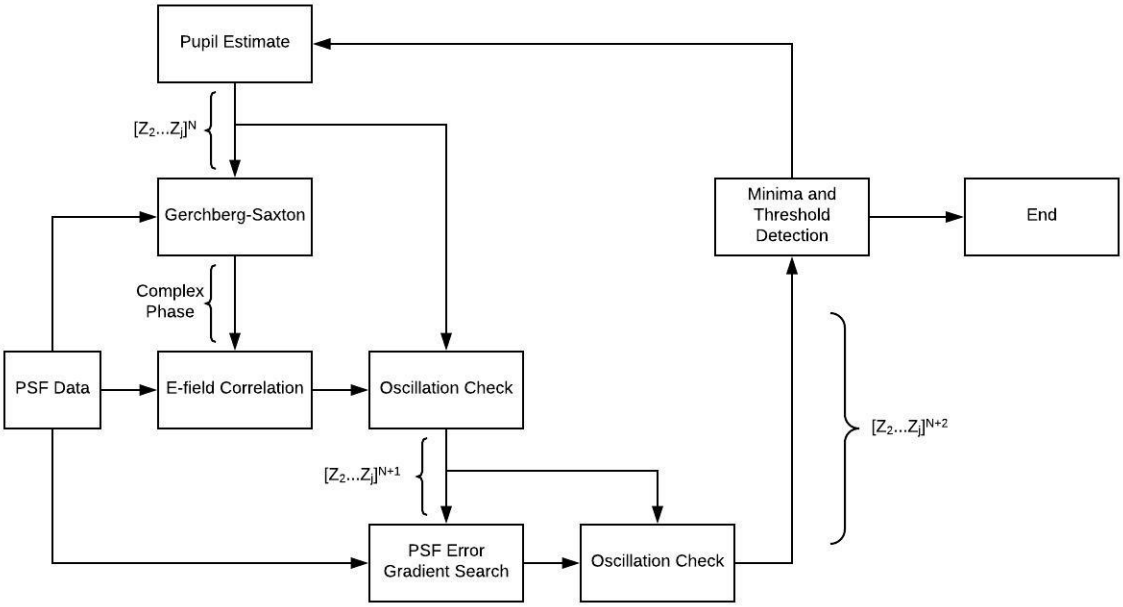

Figure 3.1. Modified PR algorithm used in this work.

The complex E-field model is then correlated with the complex E-field created by propagating a number of search pupils to the focal plane. Each Zernike coefficient of the

current pupil phase estimate is perturbed to create a stack of search pupils that deviate from the current estimate by a single search increment. Each of these search pupils is propagated to the FPA and is compared to the E-field model derived from the GS algorithm described above. The Z4 coefficient for defocus is always incremented, either positive or negative, depending on which direction gives the highest correlation. Besides the focus term, an additional Zernike coefficient is incremented based on the search pupil that yields the highest correlation coefficient. The output pupil phase coefficients (shown in Figure 3.1 as $[Z_2...Z_j]^{N+1}$) are passed to the next portion of the algorithm.

The next step in the algorithm perturbs the estimated coefficients in the same way, but computes an irradiance PSF to compare to the target PSF. Again, the two Zernike coefficient perturbations (defocus and one additional coefficient) that lead to the lowest overall residual error are added to the estimate of coefficients. This step marks the end of one iteration. The phase coefficients are either output as a final solution or they are fed back into the GS algorithm to initiate another iteration's E-field estimate. The algorithm as described in the paragraphs above is a direct implementation of work published by Zingarelli and Cain [12]. The remaining paragraphs in this section are variations added by the author.

There are two subfunctions that run in between the E-field and irradiance arms of the algorithm. The first is an oscillation check that prevents the result of one step from negating the increment of the previous step. Early studies of the algorithm showed that the estimate could get stuck in local minima by continuously adding and subtracting the same coefficients in a never-ending loop. By checking the current estimate increment against the previous increment we can prevent the short oscillation that can occur between a single coefficient. Another technique to escape these minima is by continually incrementing the focus term. The physical distance between the lens and focal plane is incredibly important to the accuracy of propagator outputs. However, measurement between the two is only possible to within a millimeter, an incredibly large distance in terms of wavelength and

phase. By forcing the algorithm to always increment a defocus term, we relax the necessity to accurately know the distance between the pupil and the FPA.

The final function is a termination function that can end the algorithm if the error between the target PSF and the estimate PSF falls below a user-selected threshold. Another way for the PSF error to end the simulation is if the current PSF error is greater than the moving average of the past 60 iterations. When this situation occurs, it is typically the result of a complicated, multi-coefficient oscillation that traps the algorithm into a poor local minima estimate.

3.2 MATLAB Implementation

3.2.1 Main GUI.

To improve usability and make analysis of the algorithm outputs simpler a Graphical User Interface (GUI) was coded in Matlab as shown in Figure 3.2. Outputs are automatically saved to a new folder timestamped to when the run was initiated. The outputs are saved in a .mat file as three separate structures. The first structure contains all simulation inputs. Only three of these inputs are accessible from the main GUI and are "Search Delta," or the increment that each Zernike coefficient is perturbed in a single iteration, the number of iterations before terminating the algorithm, and the PSF error threshold at which to terminate the algorithm. Other inputs are selected from submenus available from the main GUI and will be discussed below. The second data structure output contains the initialized pupil and the coefficients that define the starting Zernike surface. The pupil is created after pressing a button on the main GUI. Any changes to the inputs will NOT update the pupil until clicking the "create pupil" button. The last of the three data structures holds the results of the algorithm, including the final estimate, final error and E-field correlation, and a history of the evolution of all Zernike coefficients as the algorithm progresses. To run the algorithm, the user must click the "run Code" button. The algorithm will run, searching through Zernike coefficients by the defined increment until one of the end conditions has

been met. Before running the code, it is recommended to preview the pupil shape, pupil wavefront phase, and target PSF. There are no checks for valid user inputs, so the user must investigate for pupil aliasing, clipped apertures, or an anomalous target PSF. To load a measured PSF, the "Load PSF from Data" button is pushed, at which point the user will be prompted to navigate to a .mat file containing the required image. The image must be a MATLAB array of doubles that matches the size of the pupil grid. The PSF can be a single image of NxN pixels, or a stack of NxNxM images.

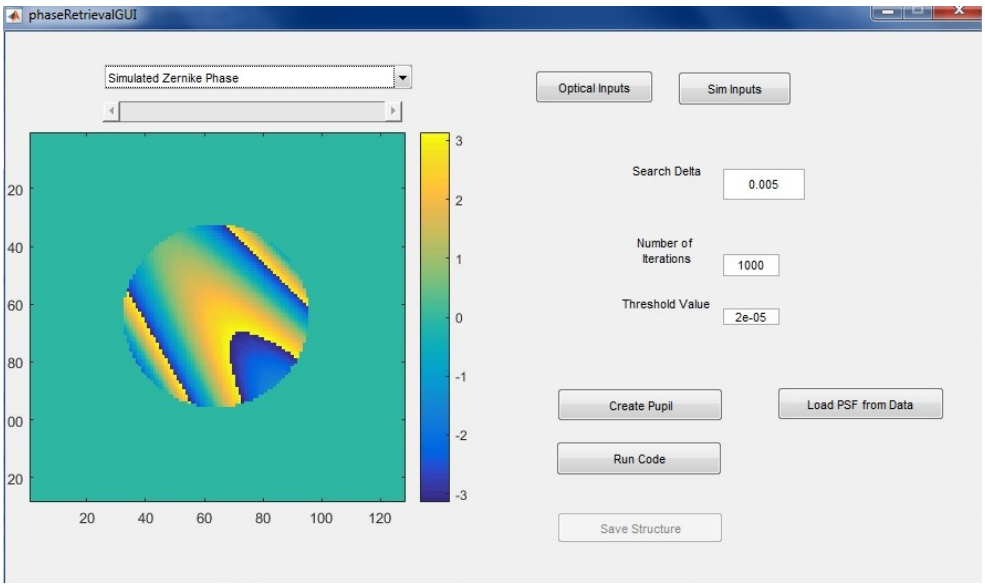

Figure 3.2. Main PR GUI showing a preview of pupil phase wavefront.

3.2.2 Input GUIs.

The first input submenu is reached by the "Optical Inputs" button and the main GUI and controls the optical parameters that create the initial pupil and is shown in Figure 3.3. Table 3.1 contains a breakdown of each input. Specific inputs were added to control for off-axis propagation at finite conjugates. The FPA must be symmetric in size and can be offset from the plane of best focus prescribed by the imaging equation. The main GUI uses

these inputs to build the initial pupil. A point source is propagated to the pupil plane from the object point described by the object distance and X and Y offsets. Then, the parabolic approximation for lens phase is applied. This phase, measured in waves, is decomposed into the desired number of Zernike coefficients. These coefficients become part of the initial pupil estimate and are passed on to the phase retrieval algorithm. This input menu also allows for the input of an additional set of Zernike coefficients to be added to the lens and source terms. This can be used to set a random pupil phase to test the algorithm's performance against simulated data. If matching to data, the user should set the Global Zernike Coefficients field to a vector of zeros, the length of which dictates the number of Zernike coefficients to use in the phase retrieval search.

The second input submenu, labeled as "Sim Inputs" on the main GUI, controls simulation specific items shown in Figure 3.4. Table 3.2 shows a description of each input available in this window. The Sim Inputs section helps control sampling in the pupil plane by varying the sample size and extent of the modeled FPA. For the results presented in this work, the experimental data used an FPA and pupil size that were in the proper regime to not require any additional sampling. If, however, the size of the modeled FPA did not sample the pupil finely enough, one could zero pad the array with additional dummy pixels. The extra pixels in the FPA would result in a finer sampling in the pupil plane. Likewise, if the size of the FPA pixels are too large then the aperture may be clipped in the pupil plane. Subsampling the FPA pixels will increase the range in the pupil and alleviate clipping. See the next section for more information on sampling requirements. The pupil can be viewed in the main GUI window to check for clipping or aliasing. This menu also defines the initialization of the pupil, either using the new off-axis propagator described in later sections, or with a flat pupil phase. A user can also add Poisson noise to the target PSF if simulating noisy imagery. The user may choose to match a single PSF, multiple simulations of the same target PSF with different initial conditions, or attempt to match a

stack of target PSFs from an image sequence. The final radio button adds a random set of Zernike coefficients to the initial pupil. The random numbers are a Gaussian draw of mean zero and $\frac{1}{2}$ variance. The randomly generated pupil phase can be used in conjunction with multiple simulations of the same target frame for sensitivity analysis of the algorithm.

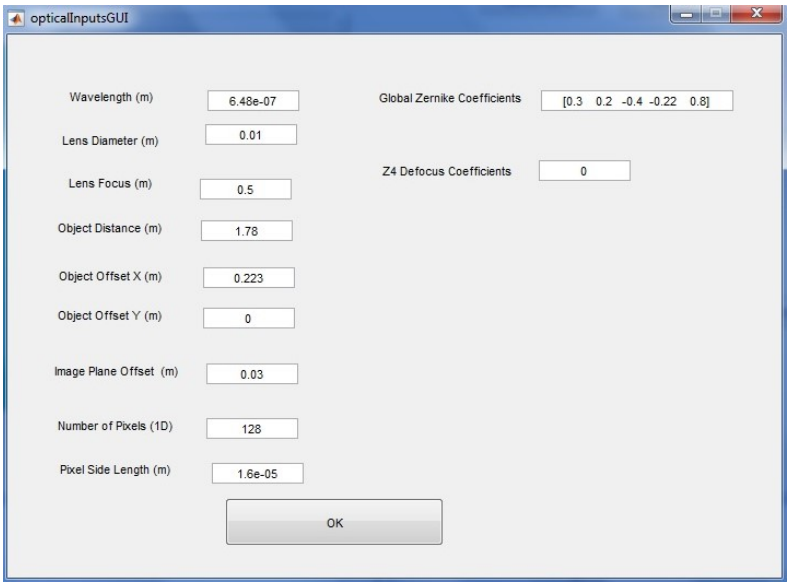

Figure 3.3. The optical setup GUI.

Table 3.1: Table of parameters in optical setup GUI

Wavelength	Wavelength of light in meters.
Lens Diameter	Diameter of clear aperture in meters.
Lens Focus	Effective Focal length in meters.
Object Distance	Distance from point source object to thin lens in meters. Positive distances and real imaging conjugates only.
Object Offset X	Translation in the x direction perpendicular from the optical axis in meters.
Object Offset Y	Translation in the Y direction perpendicular from the optical axis in meters.
Image Plane Offset	Offset of the image plane from the HARDCODED best focus value from the data collection in meters. Measured parallel to the optical axis.
Number of Pixels	Number of pixels along one edge of the modeled array. Assumed square array.
Pixel Side Length	Side length of one pixel unit cell in meters.
Global Zernike Coefficients	Desired Zernike coefficients in the pupil plane. Use these to generate target PSFs that the algorithm can attempt to estimate.
Z4 Defocus Coefficients	UNUSED, FUTURE CAPABILITY.

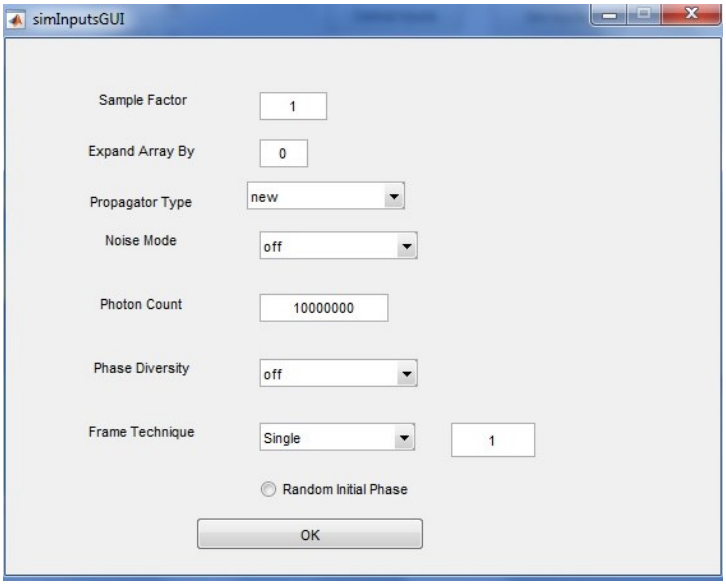

Figure 3.4. Simulation setup GUI

Table 3.2: Table of parameters in simulation setup GUI.

Sample Factor	Sub-pixel sampling resolution in the image plane. 1 corresponds to a sample size equal to pixel pitch, 2 is a sample resolution half the pixel pitch, or 4 sub-pixel samples per physical pixel. Used to expand the pupil plane and prevent clipping.
Expand Array By	Expand modeled image plane by this number of pixels on each side of the array. A value of 4 adds a 4 pixel border around the modeled array. Used to increasing sampling rate in the pupil to prevent aliasing.
Propagator Type	New: Uses the off-axis approximation for image-side phase that prevents pupil aliasing. Fresnel: Empty pupil phase with completely flat wavefront (misnomer of Fraunhofer approximation).
Noise Mode	On: add Poisson noise to the target PSF for algorithm testing purposes Off: no noise.
Photon Count	Use when Noise Mode is On. Number of photons to be distributed across the PSF.
Phase Diversity	UNUSED, FUTURE CAPABILITY.
Frame Technique	Single: If loading a PSF from data, the PSF is a single image. The number in the box to the right is the number of times to repeat the phase retrieval process on the single image. Used for multiple attempts at the same target PSF with random wavefront initialization. Stack: PSF loaded from data is a sequence of images. Images are sequentially used for target PSFs.
Random Initial Phase	Add random wavefront coefficients to the estimate initialization. Coefficients are drawn from a Gaussian distribution with μ=0 and σ^2=0.5. Draws are truncated to two decimal places.

3.3 Off-Axis Approximation

Field angles far from the optical axis of a system often contain the highest aberrations. A system may only be well corrected for a small angular region near the optical axis. Because aberrations are higher off-axis, this work explores that region to test the proposed phase retrieval algorithm. Larger pupil aberrations will result in larger PSFs and will be an easier problem for the algorithm to solve. Experimental data from an off-axis source will be used to test the algorithm.

However, as an image moves farther off-axis it imparts an additional tilt in the wavefront. For small angles, this tilt is easily sampled with a coarse digital grid. However, for higher angles, the phase of the tilted wavefront can change rapidly and induce aliasing errors in the model. While off-axis data gives good PSFs, the condition also creates a problem when attempting to model the entire pupil and FPA when using Fresnel or Fraunhofer approximations. This is particularly important when using an initial pupil phase that corresponds to the phase properties inherent in the geometry of the propagation, instead of a flat or randomly initialized pupil. If we were to use a standard Fresnel propagator for an off-axis target, the sampling required to prevent aliasing in the pupil would be cumbersome for a phase retrieval algorithm.

For the experimental data used in this paper, the image location is offset from the optical axis by 8.93cm. To model this off-axis situation with a standard Fresnel propagator, the size of the image plane must be large enough to capture the 8.93cm offset. The pupil plane will be transformed to yield the PSF in the pupil plane with the PSF appearing at the proper offset Using a pixel size of $16\mu m$, the modeled focal plane array would need to sample out to 5579 pixels from the origin to include the geometrical prediction of the PSF location. Since the image plane must be symmetric for the FFT, the total array required is over 1100 pixels on a side, which will then put the requirement for pixels to the next power of two to fully take advantage of the FFT's potential setting the array at 16,384

pixels for size. This would be an overly large array to incorporate into a PR algorithm. An observation of the required pupil phase sampling corroborates the large sample size required. Figure 3.8 shows the phase incident on the pupil from the off-axis point source. The phase spans roughly 1600 cycles across the aperture. At the current pixel spacing of 16μm, the one would need at least 10,000 by 10,000 FPA to capture the pupil phase change at a half wavelength granularity. In an FFT, the pupil and image planes have in inverse scaling relationship. If the grid that contains the pupil is larger in its physical extent, then the sampling in the image is finer. If the samples in the pupil plane are closer together, then the extent of the image plane will be larger. The relationship can be found by examining the dimensions in the Fourier kernel in Eq. (2.4). Consider Figure 3.5 where one row of two planes in an NxN FFT pair are shown. If x_{image} and x_{pupil} are the sample spacing in the image plane and pupil respectively, and Nx_{image} and Nx_{pupil} are the full spatial extents of the two planes, then $x_{image} = \frac{\lambda z}{Nx_{pupil}}$ where λ is the wavelength of the light and z is the propagation distance between planes. In summary, 10,000 pixels in image space equates to a sampling rate of $x_{pupil} = 2.89\mu\text{m} = \frac{648\text{nm}\cdot 71.25\text{cm}}{10000\text{pixels}\cdot 16\mu\text{m}}$ in the pupil plane. This pupil sampling gives roughly 3460pixels across the diameter of the 1cm aperture that can sample the tilted wavefront just above the Nyquist sampling frequency. However, with the application of another propagator, different from the Fresnel case, we are able to remove this rapidly varying phase and use a coarser, smaller grid to model the system.

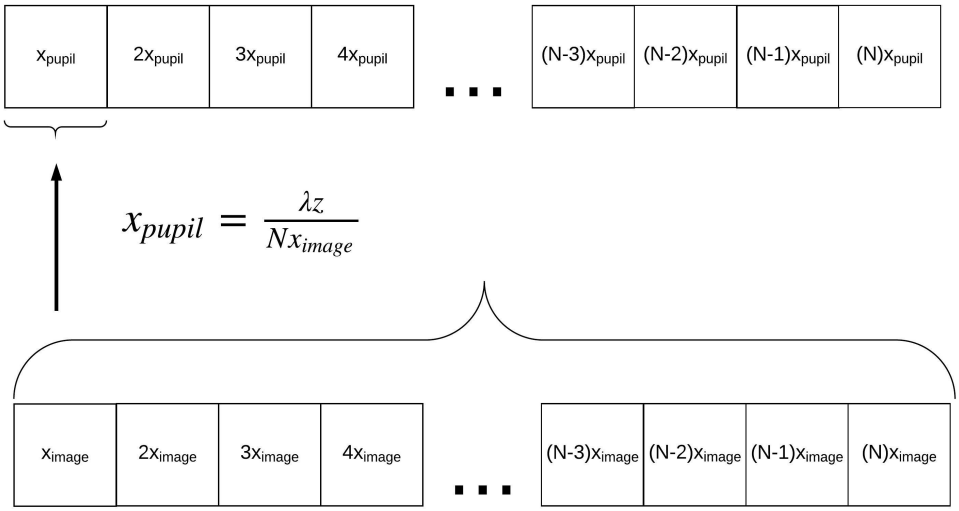

Figure 3.5. The scaled inverse spatial relationship in the FFT.

The necessary approximation can be derived by reexamining Eq. (2.2) for the distance between the pupil plane and the FPA. By offsetting the local coordinates of the pupil plane by the geometric prediction of the off-axis PSF location, $(x_2, y_2) = (x - x_0, y - y_0)$ as shown in Figure 3.6, the new distance is

$$R(\xi, \eta, x, y, z) = \sqrt{z^2 + (x - (x_0 + \xi))^2 + (y - (y_0 + \eta))^2} \tag{3.1}$$

Combining and rearranging terms gives:

$$R(\xi, \eta, x_2, y_2, z) = \sqrt{z^2 + x_2^2 + y_2^2 + \xi^2 + \eta^2 - 2x_2\xi - 2y_2\eta} \tag{3.2}$$

Expanding the distance term gives a modified version of the Fresnel propagator

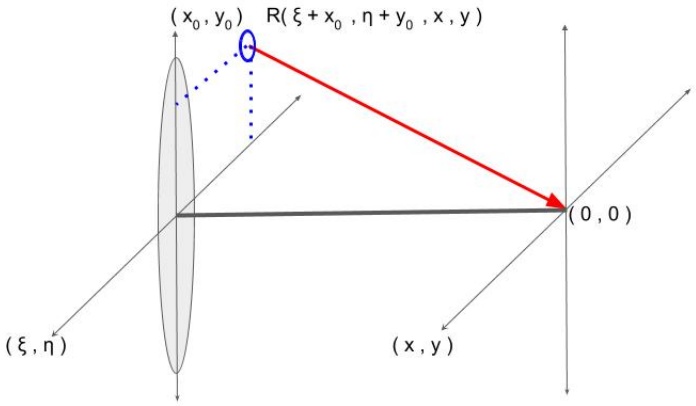

Figure 3.6. Offsetting the pupil plane coordinates by (x_0, y_0).

$$U(\xi,\eta,z) \approx \frac{1}{j\lambda z}\int_x\int_y U(x_2+x_0, y_2+y_0, 0)\ldots$$
$$\exp\left(j\pi\frac{\xi^2+\eta^2}{\lambda\sqrt{z^2+x_2^2+y_2^2}}\right)\exp\left(j2\pi\frac{\sqrt{z^2+x_2^2+y_2^2}}{\lambda}\right)\exp\left(j2\pi\frac{x_2\xi+y_2\eta}{\lambda\sqrt{z^2+x_2^2+y_2^2}}\right)dx_2dy_2 \quad (3.3)$$

Following the presentation in [2], the off-axis technique yields a different phase approximation by showing how some of the exponential terms can be altered to match the Fourier transform kernel. The first exponential term can be neglected if the quantity $\frac{\xi^2+\eta^2}{\lambda\sqrt{z^2+x_2^2+y_2^2}} << 1$. This is similar to making the leap from a Fresnel approximation to a Fraunhofer approximation, although it requires an additional step in showing how the distance term can be bounded by z as $\frac{1}{\sqrt{z^2+x_2^2+y_2^2}} < \frac{1}{z}$ and then made independent of the x_2 and y_2 coordinates. In a similar fashion the third phase term is shown to be negligibly smaller than the ideal transform kernel so that they can be interchangeable as $\frac{x_2\xi+y_2\eta}{\lambda\sqrt{z^2+x_2^2+y_2^2}} \approx \frac{x_2\xi+y_2\eta}{\lambda z}$. The second phase term is a spherical wavefront, close in structure

to the Rayleigh-Sommerfeld Propagator and opposite in sign from the typical lens phase transform. The final phase integral for the field in the FPA as used in this work is:

$$U(\xi,\eta,z) \approx \frac{1}{j\lambda z}\int_x\int_y U(x_2+x_0, y_2+y_0, 0)\exp\left(j2\pi\frac{R_0(x_2,y_2)}{\lambda}\right)\exp\left(j2\pi\frac{x_2\xi+y_2\eta}{\lambda z}\right)dx_2dy_2 \tag{3.4}$$

where the new radius term becomes:

$$R_0(x_2,y_2) = \sqrt{z^2+x_2^2+y_2^2} \tag{3.5}$$

When the offset approximation is applied, the rapidly changing phase due to an off-axis object in $U(x_2+x_0, y_2+y_0, 0)$ is mostly neutralized, leaving an easily sampled pupil. In Figure 3.8, the span of the incoming wavefront phase is easily over 1,600 waves. With a coarse sampling in the pupil, each sample has over 30 waves of difference and is completely unacceptable from an aliasing perspective. This poor sampling can be seen in the right side of Figure 3.9. However, after adding the phase from the off-axis approximation, which takes the form of the right hand side of Figure 3.8, the two wavefronts largely cancel, resulting in the left image in Figure 3.9. The off-axis approximation enables the algorithm to operate on a 128x128 array using the same sample spacing as the pixels used to capture the PSF while maintaining unaliased sampling of the pupil phase using FFT techniques. This is a particularly powerful result because with this off-axis propagator we can use direct PSF imagery without the need for supersampling or additional zero-padding to meet sampling requirements.

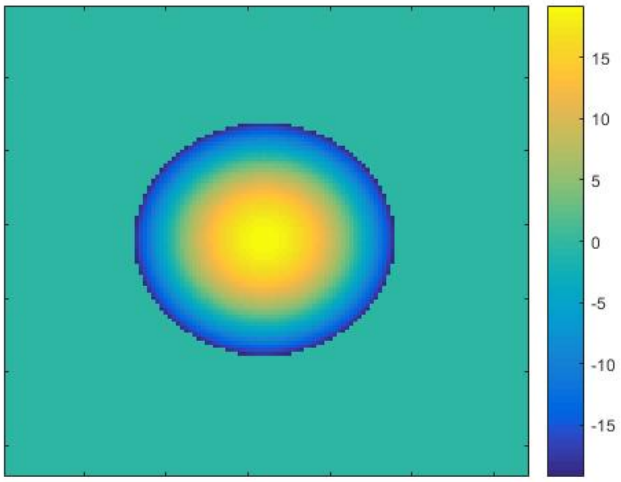

Figure 3.7. Parabolic phase front imparted by a positive focal length lens.

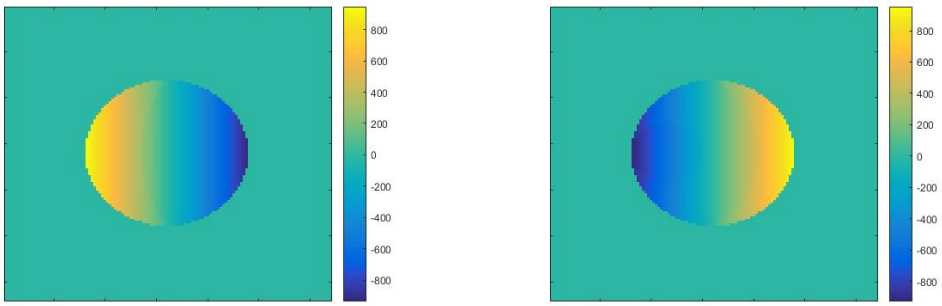

(a) (b)

Figure 3.8. (a) Strongly tilted wavefront incident on the lens from an off-axis point source, in waves. (b) Oppositely tilted wavefront of the off-axis propagation approximation, in waves.

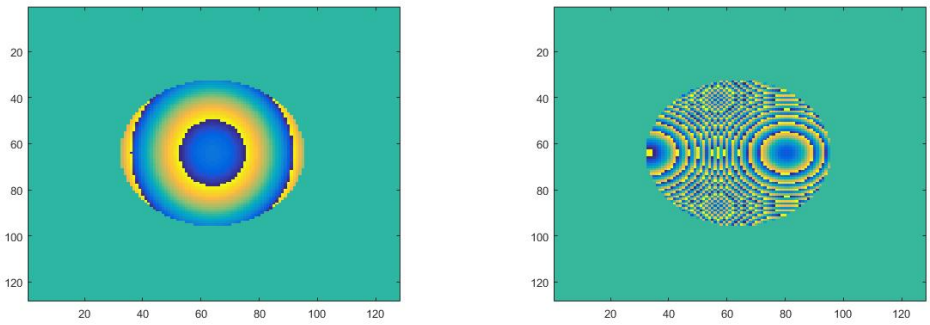

Figure 3.9. (a) Properly sampled phase front, in phase wrapped cycles from $-\pi$ to π, as a result of applying the off-axis approximation. (b) Aliased phase front of the off-axis point source only, in radians and wrapped from $-\pi$ to π

IV. Results

4.1 Synthetic PSF Retrieval

The base algorithm was verified by retrieving the pupil phase of a user-generated PSF. The PSF was generated using a Fraunhofer (flat wavefront) propagator with optical parameters that match the experimental data, discussed in the next section and shown in Figure 4.6. The PSF was created by a semi-random series of 11 Zernike polynomials (neglecting Z1, piston). Figure 4.1 shows the target PSF and the PSF generated by the algorithm's attempt to retrieve pupil phase. Although there was some randomness included in the target PSF's phase coefficients, a completely random set of 11 Zernike coefficients proved too difficult for the algorithm to retrieve. Like other algorithms, this technique was still limited by local minima solutions that could not be escaped. This algorithm typically performed better when the majority of Zernike coefficients were near zero, with only a few outlying, large aberrations. However, as in the original paper [12], the computational cost of running many instances of the algorithm from different random starting points is relatively cheap. Instead of running one long instance that is able to escape minima, one can run 100 algorithm instances with different initial coefficients in an attempt to find an optimization path free of local minima.

Also note that the algorithm is vulnerable to phase conjugation of the pupil. Although the true coefficient may be a positive term, the algorithm may select a negative term instead as the best fit. Figure 4.4 shows this twin type behavior where several of the retrieved phase coefficients have the appropriate magnitude but are opposite in sign. Figure 4.5 shows a typical error curve and E-field correlation as the algorithm nears a solution.

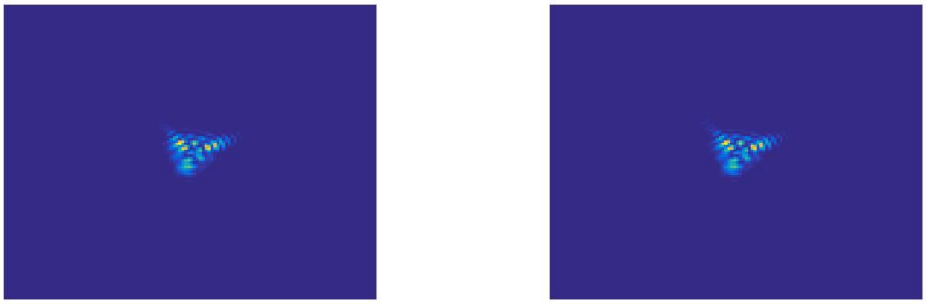

(a) (b)

Figure 4.1. (a) Synthetic PSF created from modeled phase errors. (b) Output PSF estimate from the PR algorithm.

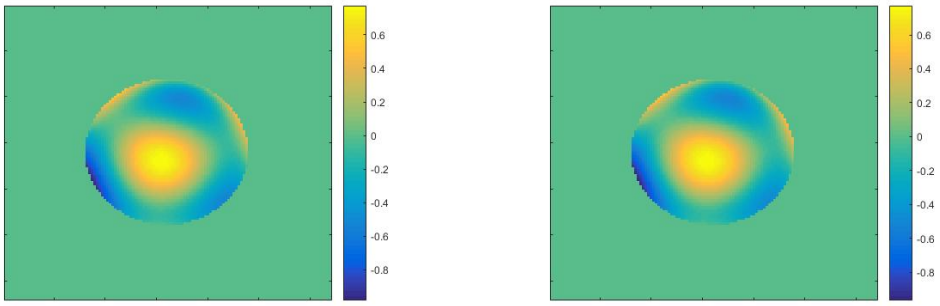

(a) (b)

Figure 4.2. (a) Synthetic truth wavefront, in waves. (b) Output wavefront estimate from the PR algorithm, in waves.

To be more effective, a smarter starting point must be chosen to have a higher probability of converging to an acceptably good solution. In some cases, using a more accurate approximation to diffraction theory could improve the estimate, for instance using a Fresnel approximation instead of a Fraunhofer. To experimentally validate the algorithm,

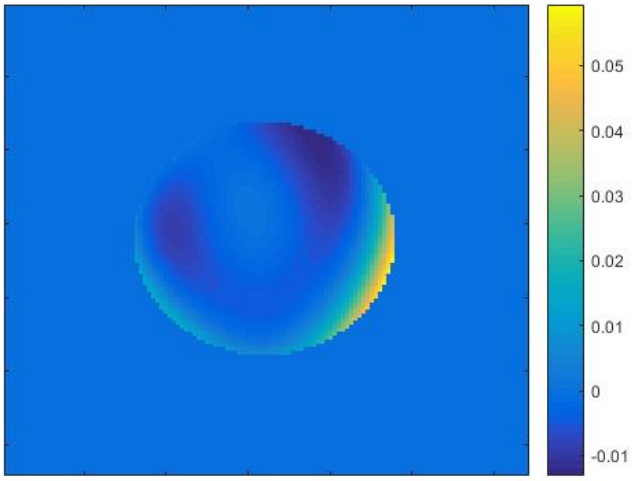

Figure 4.3. Residual wavefront error from simulations in Figure 4.2, in waves.

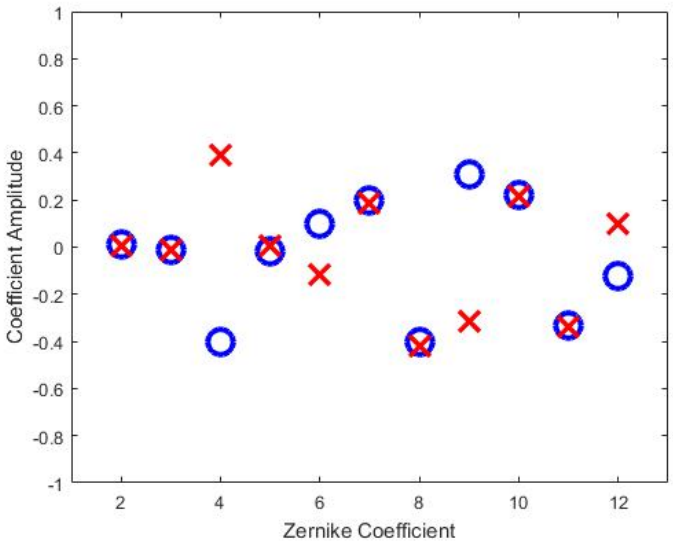

Figure 4.4. Zernike coefficients for the input and algorithm estimate. Blue is synthetic input truth and red is algorithm output.

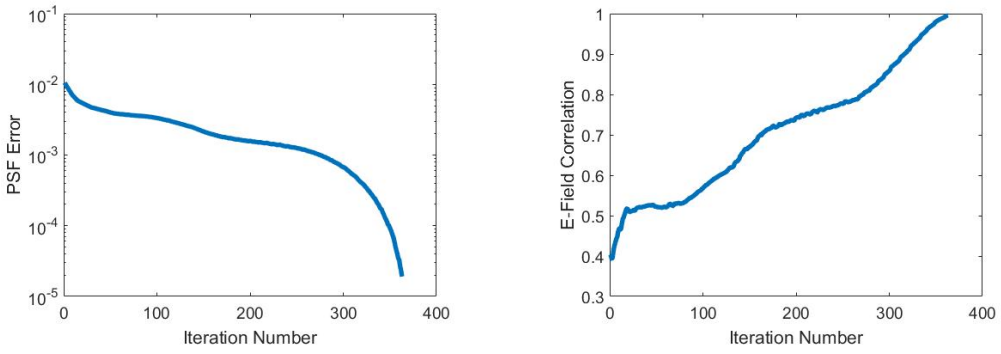

(a) (b)

Figure 4.5. (a) Sum squared error between the estimate PSF and target PSF throughout the algorithm's run time. (b) Correlation coefficient between modeled PSF E-field and estimate E-field.

a lens with known aberrations would be needed to generate experimental PSFs. Instead, data of off-axis PSFs were used since the selected singlet lens was not well-corrected for a large field angle. The degree of wavefront aberration resulting from a single lens off-axis imaging condition can be calculated from an investigation of the propagation geometry. However, a standard Fresnel approximation with an off-axis, tilted input is difficult to model discretely. By applying the off-axis approximation as a new propagator, however, one can transform an off-axis phase wavefront condition into a form easily modeled by discrete Fourier optics. Then the more accurate depiction of the initial wavefront is input into the algorithm to aid in the retrieval of pupil phase from experimental data.

4.2 Experimental Data Retrieval

The data set was collected with the setup shown in Figure 4.6 and is the same data used by Watts and Cain [2]. A 50cm focal length lens was stopped down to a clear aperture diameter of 1cm. A 648nm LED was placed in front of a small pinhole to approximate a point source. The pinhole was placed 1.78m in front of the lens and 22.3cm transverse

to the optical axis. The recording camera, with 16μm pixel pitch was set just outside of best focus at 71.25cm from the lens. This intentional defocusing yields a PSF with good features that can be used to extract pupil phase better than from a PSF taken at best focus. However, even at best focus, the chosen pixel pitch would be adequate to sample the PSF. The working F/# at this imaging conjugate is higher than at the infinite image distance case, changing from an F/# of 50 to 71.25. With a working number of 71.25 the Nyquist sampling distance in the focal plane would be 2.44λF/#, or 112μm, equating to a PSF 7 pixels in diameter. Additionally, the size of the arrays allow for proper pupil sampling. The 128x128 focal plane array of 16μm pixels translates to a pupil array extent of 2.025cm with an individual pixel sampling of 158μm. This should be an adequate pixel sampling as the pupil will be zero-padded to prevent aliasing artifacts from appearing in the digital Fourier propagation.

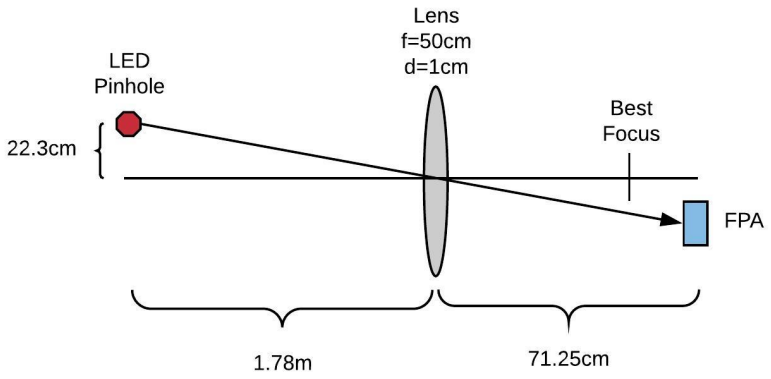

Figure 4.6. Diagram of experimental setup.

The PSF images were run through a blind deconvolution algorithm to remove the physical extent of the pinhole as performed by Zingarelli. [12]. To reduce noise, a stack of

100 raw images was averaged and was subject to a background subtraction. The cleaner, averaged imagery would be a better target for the phase retrieval algorithm. Figure 4.7 shows an example of a stack-averaged image as well as a raw frame.

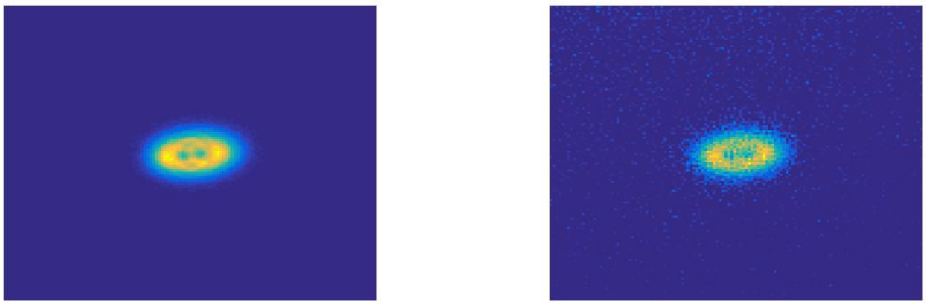

(a) (b)

Figure 4.7. (a) Experimental data image processed from the mean of 100 noisy PSF images. (b) One of the 100 noisy frames used to create the target PSF.

4.2.1 11 Zernike Coefficients.

For any phase retrieval algorithm, the success of a good estimate is dependent on a well devised initialization. A highly accurate initial estimate of pupil phase gives a high probability of algorithm convergence. For the following studies 3 different initializations were used to start the algorithm. The first initialization is the simple case of a completely flat pupil phase. This case is akin to Fraunhofer diffraction for an optical system. The second initialization was 0.5 waves of the Z4 coefficient for defocus. An analysis of the physical propagation of the geometry shows that defocus is expected to be the largest contributor to total phase in the setup. The final initialization used a phase term built up from a spherical point source, a parabolic lens transform, and the phase derived from the off-axis propagator in Eq. (3.4). This phase estimate included a significant amount of Z4

and Z5. Figure 4.8 shows the results of the algorithm with each initialization as a function of iterations. The plot shows that the new propagator is the best initialization and converges faster in both PSF error and E-field correlation than the other two conditions.

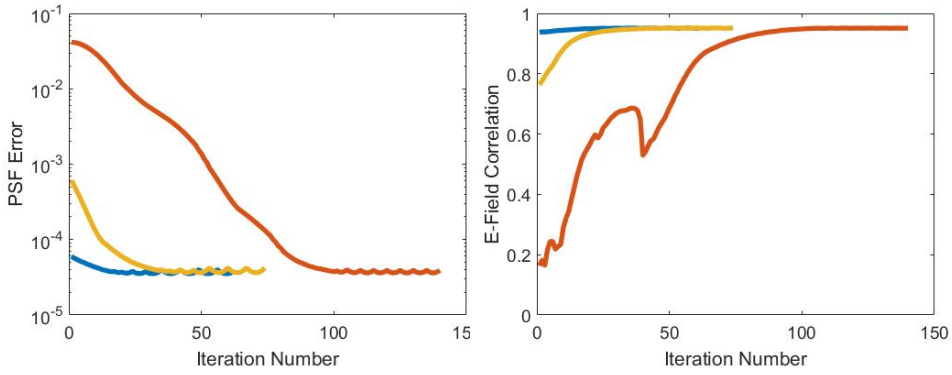

(a) (b)

Figure 4.8. (a) Sum squared error between the normalized PSF estimates and target PSF. red=flat wavefront, yellow=defocus only, blue=off-axis propagator. (b) E-field correlation coefficient between E-field model and PSF estimate.

In all cases, a modest PSF and pupil estimate are retrieved for a parametrization of 11 Zernike coefficients (Z2 through Z12). Figure 4.9 shows total pupil coefficient results for each initialization. The algorithm was able to converge very close to the same solution for each initialization case. To the human eye, the PSFs generated from the retrieved pupil phase are identical, and one example is shown in Figure 4.9. The phase coefficients plotted contain the entire phase of the system including terms inherent in the propagation geometry. A representation of the wavefront is shown in Figure 4.10. With the tight coefficient grouping in Figure 4.9, the difference in retrieved wavefront between the off-axis propagator and the defocus only case is very small, on the order of .01 waves peak to

valley (PV). The residual between the off-axis propagator and the flat pupil case is larger, on the order of 0.2 waves or greater PV. Figure 4.10 is representative of all three cases.

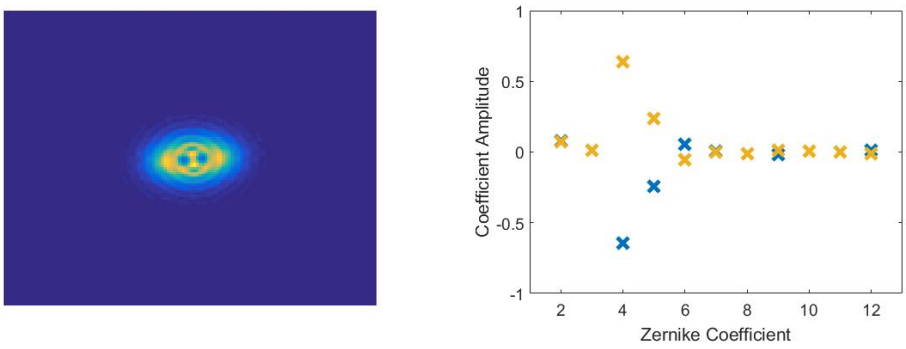

(a) (b)

Figure 4.9. (a) Final PSF estimate of the algorithm for 11 Zernike coefficients. This image is representative of all initializations. (b) Output coefficients for the three initializations, blue= off-axis propagator, yellow=defocus only, red=flat pupil. The red markers are obscured by the yellow markers.

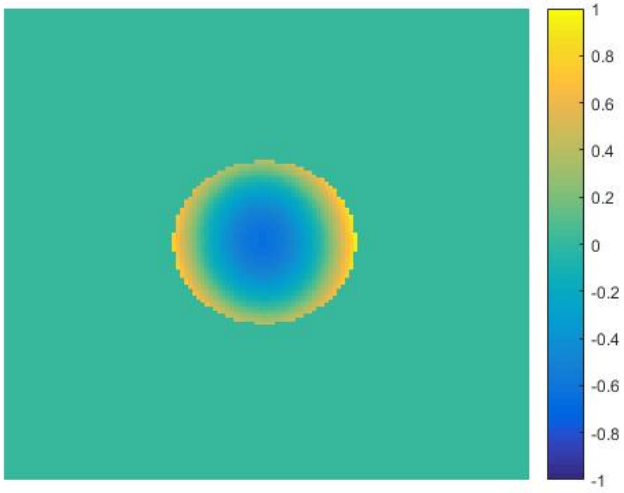

Figure 4.10. Retrieved wavefront from defocus only initialization

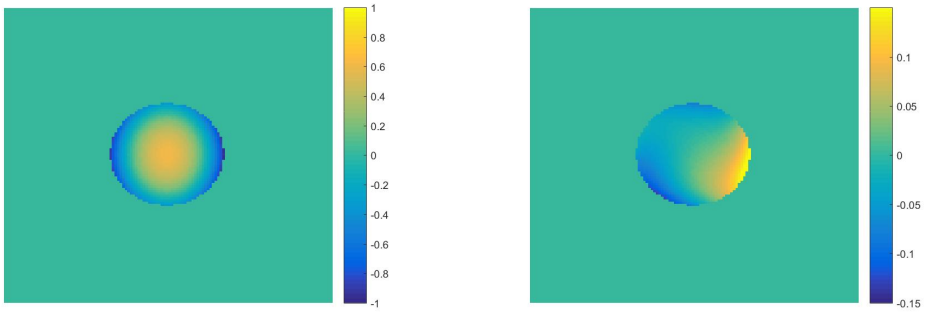

(a) (b)

Figure 4.11. (a) Initial wavefront attributed to the new propagator and source phase. (b) Additional wavefront error attributable to the lens

To find the pupil aberrations that are attributable to the lens alone, one must subtract the wavefront due to any physical effects from the propagation geometry. Figure 4.12 shows the final Zernike coefficients that can be attributed to the lens alone, given the different starting conditions. Figure 4.11 shows the wavefront for the new propagator case decomposed into the wavefront error due to propagation effects and the additional wavefront required to match the PSF. From these plots and images one is able to see that the more accurate estimate of the initial propagator gives a better estimate for the aberrations in the lens alone. If we were to make prescription changes to the lens based on retrieved phase from this single test, then the results from the flat phase initialization would drastically overcompensate. By using a good off-axis approximation, the phase distortions in the lens can be separated from those of the geometry and better correct the aberrations for a general imaging case.

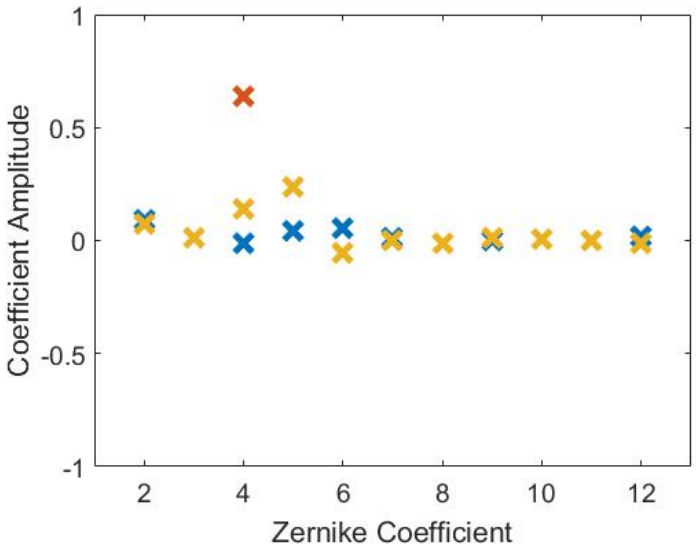

Figure 4.12. Zernike coefficients attributable to lens aberrations for each initialization. These are the coefficients in Figure 4.9 minus the initial coefficients. Red=flat wavefront, yellow=defocus only, blue=off-axis propagator.

4.2.2 48 Zernike Coefficients.

To further test the algorithm, the number of estimated Zernike coefficients was increased to 48 (Z2-Z49). The fidelity of the initialization wavefront was also increased to 48 coefficients. The final PSF solutions vary drastically for each of the 3 initial cases. Figure 4.13 shows each result of the algorithm in the different initialization conditions. It is clear that having a higher number of coefficients to choose from allows for a closer fit to the target PSF. Figure 4.14 shows the additional wavefront error in a 48 coefficient estimate when compared to an 11 coefficient estimate for the two successful initializations. In contrast, the flat pupil estimate is very bad, nowhere near a valid solution. The poor initialization got trapped in a local minima from which the algorithm could not recover.

Analyzing the algorithm's progress during each run shows some interesting behavior. First is the degree to which the flat pupil initialization underperforms when compared to the other two cases, which is easily seen in the vertical displacement of the plots in Figure 4.15. Perhaps most intriguing is that the defocus only case converges faster than the off-axis propagator. Although the defocus case reaches a solution sooner, the PSF error in the off-axis propagator is lower. In both cases the algorithm ends due to a stagnation point most likely caused by the granularity of the search increment. A more advanced version of the algorithm could switch to a finer search increment when a plateau is reached in an attempt to fine tune the estimate. As a side note, a noticeable change in slope occurs in the PSF error plot when any of the E-field coefficient plots stagnate. This could also be used to a trigger a finer search increment.

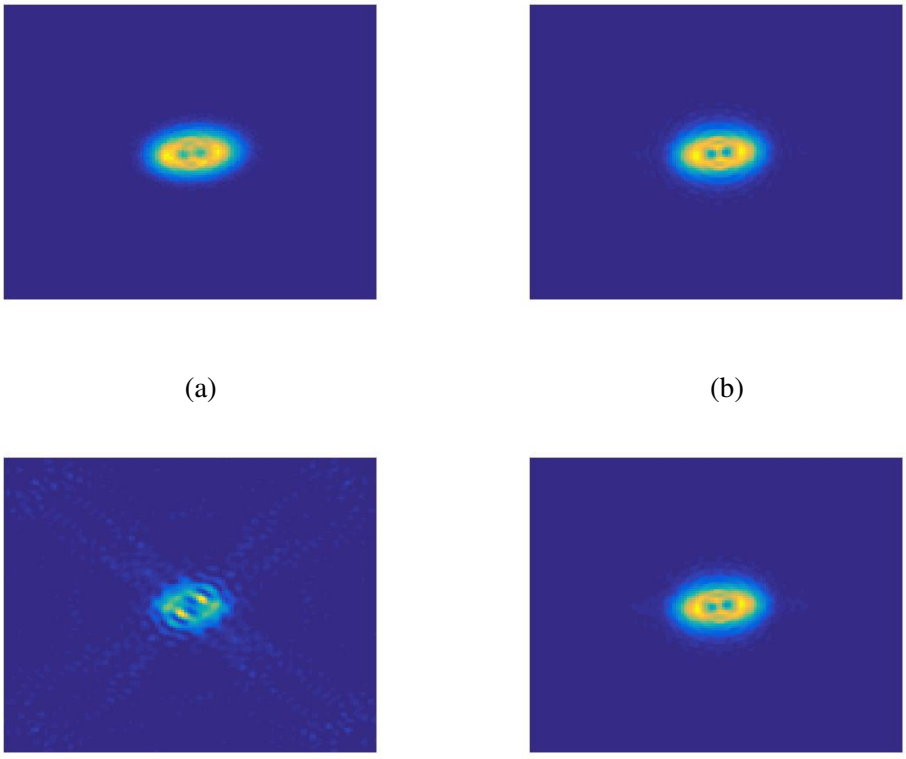

(a) (b)

(c) (d)

Figure 4.13. PSF results of the PR algorithm for various initializations parameterized by 48 Zernike coefficients.(a) Target PSF, (b) defocus only, (c) flat, (d) off-axis propagator.

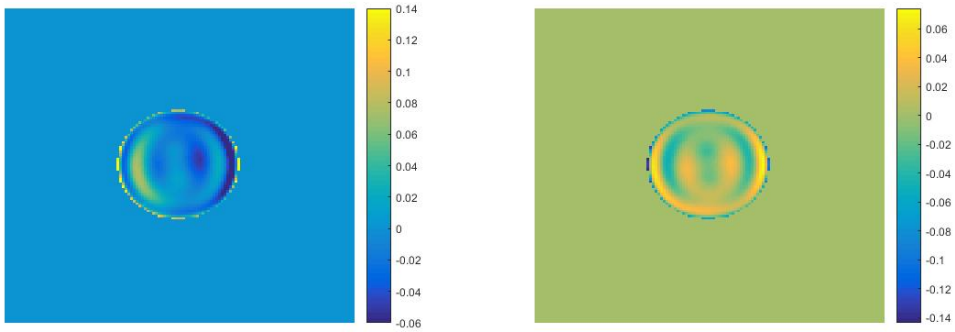

(a) (b)

Figure 4.14. Wavefront residuals between 11 retrieved coefficients and 48 coefficients for (a) the new propagator, and (b) the defocus only initialization.

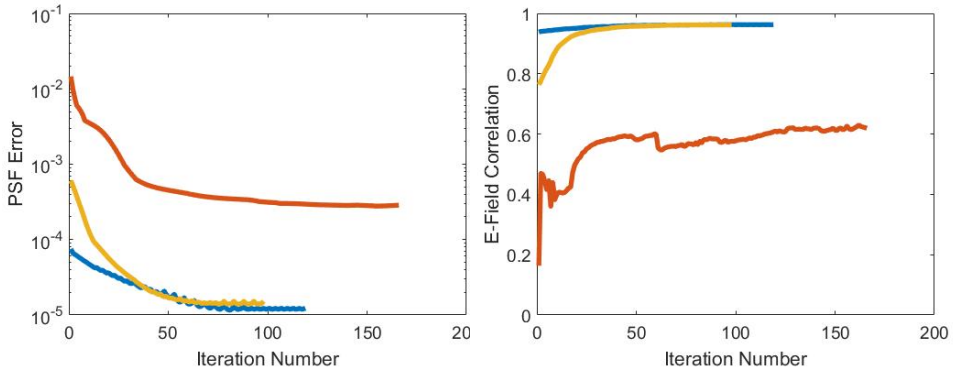

(a) (b)

Figure 4.15. (a) Sum squared error between the normalized PSF estimates and target PSF. red=flat wavefront, yellow=defocus only, blue=off-axis propagator. (b) E-field correlation coefficient between E-field model and PSF estimate.

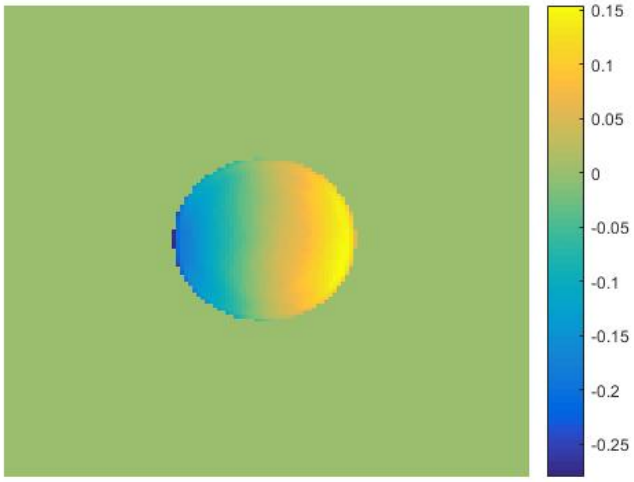

Figure 4.16. Residual of retrieved wavefronts for the new propagator and for the defocus only initialization. One wavefront has been inverted due to conjugate solutions.

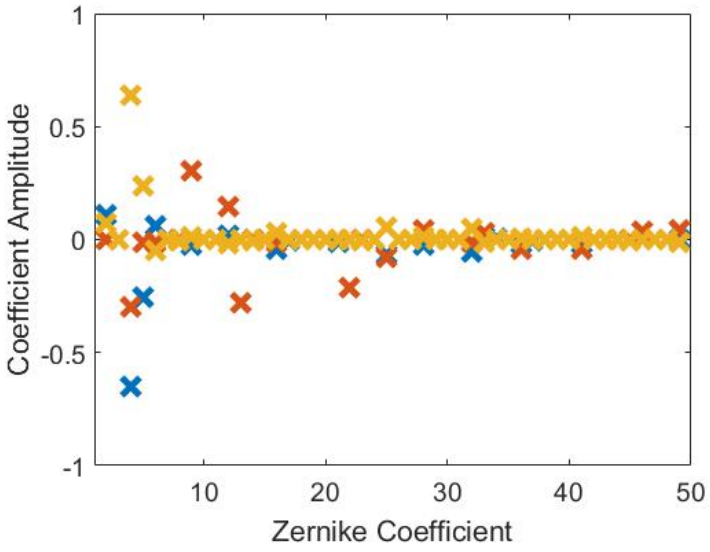

Figure 4.17. Retrieved Zernike Coefficients for the three initializations over 48 coefficients. red=flat wavefront, yellow=defocus only, blue=off-axis propagator.

4.2.3 Comparisons.

The results of the experimental phase retrieval presented in the previous section is distilled into two tables for quick comparison. 4.1 shows the number of iterations until termination, the final RSS error between the retrieved PSF and captured data, and the E-field correlation between the GS modeled field and the retrieved E-field at the algorithms termination. The initializations performed as expected in the 11 coefficient case. The slowest initialization was the flat wavefront while the fastest initialization to converge was the off-axis propagator by over a factor of 2. The errors and correlations in the 11 coefficient case are closely spaced, as each initialization closed in on similar solutions.

Moving on to the 48 coefficient case, 4.2 shows some interesting behavior. The flat propagator failed to converge to a useful solution and terminated due to stagnant error in a local minimum. While the defocus only case converged and terminated sooner than the off-axis case, it did not result in a lower error term. The defocus only case quickly reached a minima but was unable to push lower, as the off-axis initialization did. This could be because the defocus only case was initialized with a positive half wave of defocus, biasing the solution in an opposite direction from the negative defocus term retrieved from the off-axis solution. It is clear from the data that incorporating a better initial estimate with the off-axis propagator improves performance of the algorithm.

Table 4.1: Initialization Comparison for 11 Coefficients

Initialization	**Iterations**	**RSS Error**	**E-Field Correlation**
Flat	140	3.92e-5	0.9511
Defocus Only	74	4.20e-5	0.9516
Off-Axis	62	3.76-5	0.9512

Table 4.2: Initialization Comparison for 48 Coefficients

Initialization	**Iterations**	**RSS Error**	**E-Field Correlation**
Flat	166	2.86e-4	0.6195
Defocus Only	98	1.52e-5	0.9619
Off-Axis	119	1.23e-5	0.9630

V. Conclusion

A phase retrieval algorithm has been reimplemented to take advantage of an off-axis propagation approximation for faster, more efficient estimates of pupil phase. The algorithm is laid out in Section 3.1 and the benefit of incorporating the off-axis propagator is shown in Section 3.3. The tool has been developed into a MATLAB GUI, outlined in section 3.2, for easy synthesis and analysis of data. Section 4.1 shows the retrieval of pupil phase from a simulated PSF while finding the proper magnitude of the simulated aberrations, although in some cases of the wrong sign. The final tool is able to incorporate phase initializations that match theoretical phase conditions at finite imaging conjugates without a burdensome sampling rate or array size as shown in Section 4.2. The experimental data shows that the initiliazed wavefront error has an impact on the number of iterations required to find a suitable solution, further highlighting the importance of the off-axis propagator.

This work could be expanded in several ways. First, the user experience and GUI appearance could be improved if the work were to become a disseminated product. To increase the flexibilty of the algorithm, a simple addition of more Zernike coefficients could be integrated, although without additional development the run time of the algorithm may suffer due to the larger search space. On that note, the algorithm could be optimized to minimize calculations on large arrays and have better memory management for resource-limited computing systems. Long term additions to the algorithm could develop an advanced minima detection algorithm that can sense local minima, and ”back out” to an earlier estimate, and then perturb the estimate to force a new path. Lastly, the algorithm could be expanded to support multiple images incorporating phase diversity for a more robust algorithm. While phase diversity was initially investigated in this work, it was eventually abandoned due to the growing scope of the project.

Appendix: MATLAB Code

Available upon request: salome.carrasco@us.af.mil

Bibliography

[1] "First Hubble Space Telescope WFPC-II Images". https://www.noao.edu/hubble/wfpcII.press.html, January 1994.

[2] Cain, Stephen C. and Tatsuki Watts. "Nonparaxial Fourier propagation tool for aberration analysis and point spread function calculation". *Optical Engineering*, 55(8):085104, 2016. ISSN 0091-3286.

[3] Fienup, J. R. "Phase-retrieval algorithms for a complicated optical system". *Applied Optics*, 32(10):1737, 1993. ISSN 0003-6935.

[4] Fienup, J R, J C Marron, T J Schulz, and J H Seldin. "Hubble Space Telescope characterized by using phase-retrieval algorithms." *Applied optics*, 32(10):1747–1767, 1993. ISSN 0003-6935.

[5] Fienup, James R. "Wave Front Sensing by Nonlinear Optimization". 2769(1982):14627, 1999. ISSN 21622701.

[6] Fienup, James R. "Phase retrieval algorithms: a personal tour [Invited]". *Applied Optics*, 52(1):45–56, 2012. ISSN 1539-4522.

[7] Gerchberg, R W and W O Saxton. "A practical algorithm for the determination of phase from image and diffraction plane pictures". *Optik*, 35(2):237–246, 1972. ISSN 10500529.

[8] Gonsalves, Robert A. "Perspectives on phase retrieval and phase diversity in astronomy". *SPIE Astronomical Telescopes + Instrumentation*, 9148:91482P, 2014. ISSN 1996756X.

[9] Goodman, J.W. *Introduction to Fourier Optics*. MaGraw-Hill, 2nd edition, 1996.

[10] Noll, Robert J. "Zernike polynomials and atmospheric turbulence*". 06856(October 1975):207–211, 1976.

[11] Shechtman, Yoav, Yonina C. Eldar, Oren Cohen, Henry N. Chapman, Jianwei Miao, and Mordechai Segev. "Phase Retrieval with Application to Optical Imaging". (April 2015):1–25, 2014. ISSN 1053-5888.

[12] Zingarelli, John C and Stephen C Cain. "Phase retrieval and Zernike decomposition using measured intensity data and the estimated electric field". *Applied Optics*, 52(31):7435, 2013. ISSN 0003-6935.

REPORT DOCUMENTATION PAGE

Form Approved
OMB No. 0704–0188

1. REPORT DATE *(DD–MM–YYYY)*	2. REPORT TYPE	3. DATES COVERED *(From — To)*
14–06–2018	Master's Thesis	Apr 2014–Jun 2018

4. TITLE AND SUBTITLE

Efficient Phase Retrieval for Off-Axis Point Spread Functions

5a. CONTRACT NUMBER

5b. GRANT NUMBER

5c. PROGRAM ELEMENT NUMBER

6. AUTHOR(S)

Carrasco, S. Esteban, CIV DR-II, USAF

5d. PROJECT NUMBER

5e. TASK NUMBER

5f. WORK UNIT NUMBER

7. PERFORMING ORGANIZATION NAME(S) AND ADDRESS(ES)

Air Force Institute of Technology
Graduate School of Engineering and Management (AFIT/EN)
2950 Hobson Way
WPAFB, OH 45433-7765

8. PERFORMING ORGANIZATION REPORT NUMBER

AFIT-ENG-MS-18-J-084

9. SPONSORING / MONITORING AGENCY NAME(S) AND ADDRESS(ES)

INTENTIONALLY LEFT BLANK

10. SPONSOR/MONITOR'S ACRONYM(S)

11. SPONSOR/MONITOR'S REPORT NUMBER(S)

12. DISTRIBUTION / AVAILABILITY STATEMENT

DISTRIBUTION STATEMENT A:
APPROVED FOR PUBLIC RELEASE; DISTRIBUTION UNLIMITED

13. SUPPLEMENTARY NOTES

14. ABSTRACT

A novel pairing of phase retrieval tools allows for efficient estimation of pupil phase in optical systems from images of point spread functions (PSFs). The phase retrieval algorithm uses correlation of modeled phase in the focal plane to decouple aberrations that are difficult to identify in complex PSFs. The use of a phase kernel that departs from the Fresnel approximation for off-axis PSFs is a more accurate representation of wavefront phase in finite conjugate imaging. The combination of the approximation and phase correlation algorithm can be more efficient and accurate than generic algorithms.

15. SUBJECT TERMS

Phase retrieval, optical aberrations, point spread function, Fourier optics

16. SECURITY CLASSIFICATION OF:			17. LIMITATION OF ABSTRACT	18. NUMBER OF PAGES	19a. NAME OF RESPONSIBLE PERSON
a. REPORT	b. ABSTRACT	c. THIS PAGE			Dr. Stephen Cain (ENG)
U	U	U	UU	63	19b. TELEPHONE NUMBER *(include area code)* (937) 255-3636 x4716 Stephen.Cain@afit.edu